

Bayesian Inversion for Nonlinear Imaging Models using Deep Generative Priors

Pakshal Bohra, Thanh-an Pham, Jonathan Dong and Michael Unser, *Fellow, IEEE*

Abstract—Most modern imaging systems incorporate a computational pipeline to infer the image of interest from acquired measurements. The Bayesian approach for solving such ill-posed inverse problems involves the characterization of the posterior distribution of the image. This depends on the model of the imaging system and prior knowledge on the image of interest. In this work, we present a Bayesian reconstruction framework for nonlinear imaging models, where the prior knowledge on the image is specified by a deep generative model. We develop a tractable posterior sampling scheme based on the Metropolis-adjusted Langevin algorithm (MALA) for the class of nonlinear inverse problems where the forward model has a neural-network-like structure. This class includes most practical imaging modalities. We introduce the notion of augmented deep generative priors in order to suitably handle quantitative image recovery. We illustrate the advantages of our framework by applying it to two nonlinear imaging modalities—phase retrieval and optical diffraction tomography.

Index Terms—Bayesian inference, nonlinear inverse problems, phase retrieval, optical diffraction tomography, deep learning, neural networks, generative models, generative adversarial networks.

I. INTRODUCTION

In practical imaging systems, the object of interest $\mathbf{s} \in \mathbb{R}^K$ is observed indirectly by performing a series of measurements $\mathbf{y} \in \mathbb{C}^M$. Mathematically, this process is often modelled as

$$\mathbf{y} = \mathbf{H}(\mathbf{s}) + \mathbf{n}, \quad (1)$$

where $\mathbf{H} : \mathbb{R}^K \rightarrow \mathbb{C}^M$ is an operator that describes the physics of the imaging system and $\mathbf{n} \in \mathbb{C}^M$ is an additive noise. The operator \mathbf{H} can be linear or nonlinear, depending on the imaging modality. For example, in magnetic resonance imaging (MRI), one captures noisy samples of the Fourier transform of the signal. The task at hand is then to reconstruct the signal \mathbf{s} from the obtained measurements \mathbf{y} . Typically, such inverse problems are ill-posed in the sense that there exist a multitude of signals which produce similar measurements. Thus, we cannot rely on direct inversion techniques to obtain relevant solutions.

This work was supported in part by the Swiss National Science Foundation under Grant 200020_184646 / 1 and in part by the European Research Council (ERC Project FunLearn) under Grant 101020573. The authors are with the Biomedical Imaging Group, École polytechnique fédérale de Lausanne, 1015 Lausanne, Switzerland (e-mail: pakshal.bohra@epfl.ch; thanh-an.pham@epfl.ch; jonathan.dong@epfl.ch; michael.unser@epfl.ch).

A. Variational Methods

In variational methods, the solution to the inverse problem is specified as the minimizer of a cost functional

$$\hat{\mathbf{s}} = \arg \min_{\mathbf{s} \in \mathbb{R}^K} \left(E(\mathbf{y}, \mathbf{H}(\mathbf{s})) + \tau R(\mathbf{s}) \right), \quad (2)$$

where the data-fidelity term $E : \mathbb{C}^M \times \mathbb{C}^M \rightarrow \mathbb{R}_+$ forces the solution to be consistent with the measurements, the regularization $R : \mathbb{R}^K \rightarrow \mathbb{R}_+$ imposes some prior constraints about the signal of interest on the solution, and $\tau \in \mathbb{R}_+$ is a tunable hyperparameter. Typical candidates for these terms are $E(\mathbf{y}, \mathbf{H}(\mathbf{s})) = \|\mathbf{y} - \mathbf{H}(\mathbf{s})\|_2^2$ and $R(\mathbf{s}) = \|\mathbf{L}\mathbf{s}\|_p^p$ [1]–[7] with $p \in [1, 2]$. Here, \mathbf{L} is a linear transformation such as the discrete version of the wavelet transform or the gradient operator, which takes part in the regularization. For instance, total-variation (TV) regularization [3] uses the ℓ_1 -norm along with the gradient operator, which promotes solutions with sparse derivatives. It is widely used for compressed sensing and extreme imaging applications where the data is scarce [7]. The resulting optimization problems are typically solved by iterative algorithms such as gradient descent, ISTA/FISTA [8]–[10] or ADMM [11].

B. Bayesian Inference

In the Bayesian approach to image reconstruction [12]–[15], the signal \mathbf{s} is modelled as a realization of a random vector with a suitable probability density function (pdf) p_S that captures our prior knowledge about the signal. The idea here is to characterize the posterior distribution

$$p_{S|Y}(\mathbf{s}|\mathbf{y}) \propto p_N(\mathbf{y} - \mathbf{H}(\mathbf{s}))p_S(\mathbf{s}), \quad (3)$$

which depends on the statistics of the noise p_N and the prior distribution p_S , and to make inferences based on it.

The posterior distribution can be used for the derivation of several point estimators for the signal \mathbf{s} . One such example is the maximum a posteriori (MAP) estimator, which is the mode of the posterior distribution. The MAP estimator leads to an optimization problem that resembles (2), with $E(\mathbf{y}, \mathbf{H}(\mathbf{s})) \propto (-\log(p_N(\mathbf{y} - \mathbf{H}(\mathbf{s}))))$ and $R(\mathbf{s}) \propto (-\log(p_S(\mathbf{s})))$, and thus links the variational and Bayesian approaches [16]–[18]. Another example is the minimum mean square error (MMSE) estimator which turns out to be the posterior mean.

Besides the derivation of point estimators, the Bayesian framework allows us to quantify the uncertainty of the reconstructed image. This feature offers an interesting perspective for computational imaging as most practical reconstruction

schemes, including the variational ones, do not provide any assessment of reliability.

In general, performing such inference tasks entails the estimation of expected values with respect to the posterior distribution. Typically, these are high-dimensional integrals that cannot be evaluated analytically. Thus, one relies on Markov Chain Monte Carlo (MCMC) methods to efficiently draw samples from the posterior and then uses them to approximate the integrals [19]–[22].

C. Deep Learning Based Methods

Over the past few years, researchers have started deploying deep-learning-based methods for solving inverse problems in imaging. The learning-based methods have been found to outperform the traditional model-based ones. Broadly speaking, their underlying principle is to utilize large amounts of training data to improve the reconstruction quality instead of prespecifying prior information about the image of interest in the form of mathematical models, as in the variational and Bayesian approaches described earlier.

The first generation of deep-learning-based methods involve training a convolutional neural network (CNN) as a nonlinear mapping that relates a low-quality estimate of the signal to the desired high-quality estimate [23]–[27]. The reconstruction pipeline then consists of using a fast classical algorithm to yield an initial solution and then correcting for its artifacts using the trained CNN. This category of methods includes “unrolling” [28]–[33], where the architecture of the CNN is designed by studying iterations of algorithms used for solving Problem (2). While these first generation end-to-end learning methods have achieved state-of-the-art performances in several inverse problems, recent works have highlighted their instability and lack of robustness [34], [35].

The second generation of deep-learning-based methods aim to integrate CNNs into iterative reconstruction algorithms. The Plug-and-Play priors (PnP) [36] and Regularization-by-Denoising (RED) [37] frameworks are two successful examples that provide a way to carry out this integration. In PnP algorithms, the proximal operator appearing in iterations of proximal algorithms (FISTA, ADMM) is replaced by a generic denoiser which represents an implicit prior on the signal. RED, by contrast, incorporates an explicit regularization term that is constructed with the help of the chosen denoiser. In the learning-based variants of these frameworks, one uses appropriately trained CNNs as the denoising routines [38]–[44]. Another example of such methods is projected gradient descent where the projection operator is a trained neural network that projects onto the space of desired signals [45]–[47]. Unlike the first generation methods, the second generation ones enforce consistency between the reconstructed signal and the acquired measurements. They are also more versatile as the CNN denoisers can be used for different kinds of inverse problems without the need for retraining. The difficulty in employing these learning-based iterative schemes is that the Lipschitz constant of the CNNs must be controlled in order to ensure their convergence [48], [49], which is not straightforward and remains an active area of research [49]–[51].

One can also identify a third class of deep-learning-based methods that make use of deep generative models such as variational autoencoders (VAE) [52] and generative adversarial networks (GAN) [53]. These models include a generator network that map a low-dimensional latent space to the high-dimensional signal space. They are trained to capture the statistics of the dataset and generate sample signals similar to those in the dataset. Once such a deep generative model has been successfully trained, its application to an inverse problem typically consists of finding the optimal latent variable such that the resulting signal best fits the measurements. Recent works have focused on designing and analyzing algorithms for the task of inverting such generative models [54]–[57].

The three classes of deep-learning-based methods that we have discussed so far are variational in nature and they provide a single reconstruction as the output. Given the success of these methods, there has naturally been interest in developing Bayesian methods that exploit the power of neural networks. For instance, in [58], the authors propose two frameworks for “deep Bayesian inversion” that are analogs of the first generation end-to-end deep-learning-based methods and require training data consisting of signals and their corresponding measurements. Their first approach involves training a conditional GAN to sample from the posterior distribution while their second approach uses neural networks to approximate a chosen statistical estimator. More recently, the focus has been on developing more modular Bayesian methods where only the prior is modelled by neural networks. This has led to the development of various posterior sampling schemes for priors that are defined either implicitly through denoising CNNs (such as the ones used in the PnP or RED frameworks) [59]–[61] or through GANs [62], VAEs [63], [64] and score-based generative models [65], [66]. So far, most of these works have focused on inverse problems with linear or linearized forward models.

A current frontier in imaging is the inversion of nonlinear models, which arise in several applications, with two notable examples being phase retrieval and optical diffraction tomography. Such applications could benefit greatly from the development of neural-network-based Bayesian reconstruction methods.

D. Contributions

In this paper, we present a Bayesian framework for solving a broad class of nonlinear inverse problems, where the prior on the image of interest is represented by a trained deep generative model. Our contributions are as follows:

- We develop a method based on the Metropolis-adjusted Langevin Algorithm (MALA) [67], [68] to sample from the posterior distribution for the class of nonlinear inverse problems where the forward model has a neural-network-like structure. This class includes a wide variety of practical imaging modalities. We show that the structure of the forward model and the low-dimensional latent space of the generative prior enable tractable Bayesian inference.
- We introduce the concept of augmented generative models. This is motivated by the observation that deep

generative models are easier to train when the dataset consists of images with the same range of pixel values. Unfortunately, such models are not well-matched to imaging modalities where one is interested in extracting the absolute intensity of objects rather than merely visualizing contrast. Our proposed augmented models provide us with a simple but effective way of overcoming the aforementioned problem.

- We illustrate the advantages of the proposed reconstruction framework with the help of numerical experiments for two nonlinear imaging modalities—phase retrieval and optical diffraction tomography.

The paper is organized as follows: In Section II, we discuss the structure of the forward model for our nonlinear inverse problems. We detail the Bayesian reconstruction framework in Section III. There, we introduce augmented generative models and we explain our posterior sampling scheme. We present our experimental results in Section IV.

II. NONLINEAR INVERSE PROBLEMS: FORWARD MODELS

In this section, we briefly describe the class of nonlinear inverse problems that we are interested in. We then focus on two concrete examples—phase retrieval and optical diffraction tomography—and detail the physical models involved.

A. Nonlinear Inverse Problems

The objective is to recover an image $\mathbf{s} \in \mathbb{R}^K$ from its noisy measurements $\mathbf{y} \in \mathbb{C}^M$ given by $\mathbf{y} = \mathbf{N}(\mathbf{y}_0)$ with

$$\mathbf{y}_0 = \mathbf{H}(\mathbf{s}), \quad (4)$$

where $\mathbf{H} : \mathbb{R}^K \rightarrow \mathbb{C}^M$ is a nonlinear operator that models the physics of the imaging system and $\mathbf{N} : \mathbb{C}^M \rightarrow \mathbb{C}^M$ is an operator that models the corruption of the measurements by noise. In this work, we consider the class of nonlinear forward models \mathbf{H} whose computational structure can be encoded by a directed acyclic graph and thus resembles a neural network.

The Jacobian matrix of \mathbf{H} at any point $\mathbf{x} = (x_1, \dots, x_K) \in \mathbb{R}^K$ is defined as

$$\mathbf{J}_{\mathbf{H}}(\mathbf{x}) = \begin{bmatrix} \frac{\partial}{\partial x_1} [\mathbf{H}(\mathbf{x})]_1 & \cdots & \frac{\partial}{\partial x_K} [\mathbf{H}(\mathbf{x})]_1 \\ \vdots & \vdots & \vdots \\ \frac{\partial}{\partial x_1} [\mathbf{H}(\mathbf{x})]_M & \cdots & \frac{\partial}{\partial x_K} [\mathbf{H}(\mathbf{x})]_M \end{bmatrix}. \quad (5)$$

Gradient-based MCMC methods (see Section III for a specific example) involve computing quantities such as $\mathbf{J}_{\mathbf{H}}^H(\mathbf{x})\mathbf{r}$ for some vectors $\mathbf{x} \in \mathbb{R}^K$, $\mathbf{r} \in \mathbb{C}^M$, and this can be a potential bottleneck. The neural-network-like structure of \mathbf{H} allows us to compute these efficiently using the error backpropagation algorithm. This, in turn, makes tractable Bayesian inference computationally feasible.

The class of nonlinear inverse problems that fit this description is very broad and adaptable to most existing imaging modalities. In principle, it covers all possible inverse problems. The linear case is trivially covered. More generally, if sufficient data is available, one can rely on the universal approximation property of neural networks and train such a system to mimic the physics of our forward model. Next, we look at two particular problems that nicely fall within our predefined class.

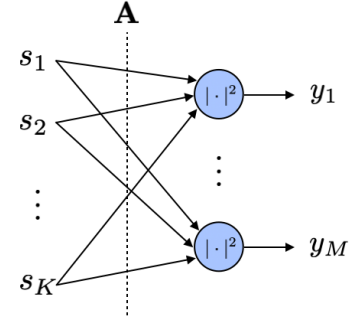


Fig. 1: The forward model for phase retrieval (6) expressed as a one-layer fully-connected neural network with linear weights \mathbf{A} and quadratic activation functions.

B. Phase Retrieval

Phase retrieval [69], [70] is a prevailing nonlinear inverse problem that is ubiquitous in computational imaging. The aim there is to recover a signal from its intensity-only measurements which is a central issue in optics [71], [72], astronomy [73], [74] and computational microscopy [75]–[78].

In the phase retrieval problem that we consider in this paper, the noise-free measurements are modelled as

$$\mathbf{y}_0 = \mathbf{H}_{\text{pr}}(\mathbf{s}) = |\mathbf{A}\mathbf{s}|^2, \quad (6)$$

where $\mathbf{A} : \mathbb{R}^K \rightarrow \mathbb{C}^M$ is either the Fourier matrix [71], [78], [79] or a fixed random matrix with independent and identically distributed (i.i.d.) elements [70], [80], [81], and $|\cdot|^2$ is a component-wise operator. As shown in Figure 1, the forward model in (6) can be expressed as a one-layer fully-connected neural network with fixed linear weights \mathbf{A} and quadratic activation functions.

C. Optical Diffraction Tomography

In optical diffraction tomography (ODT), the aim is to recover the refractive index (RI) map of a sample from complex-valued measurements of the scattered fields generated when the sample is probed by a series of tilted incident fields [82]. According to the scalar diffraction theory, the propagation of the incident fields through the sample is governed by the wave equation. While pioneering works relied on linear models to approximate the field propagation [82], [83], recent works have significantly improved the quality of RI reconstruction by using more accurate nonlinear models which account for multiple scattering [84]. Here, we look at one such nonlinear model called the Beam Propagation Method (BPM).

Helmholtz Equation: We consider a sample with a real-valued spatially varying refractive index that is immersed in a medium with refractive index n_b , as shown in Figure 2. The refractive index distribution in our region of interest $\Omega = [0, L_x] \times [0, L_z]$ is represented as $n(\mathbf{r}) = n_b + s(\mathbf{r})$, where $\mathbf{r} = (x, z)$ and $s(\mathbf{r})$ is the refractive index contrast. The sample is illuminated with an incident plane wave $u^{\text{in}}(\mathbf{r})$ of free space wavelength λ , whose direction of propagation is specified by

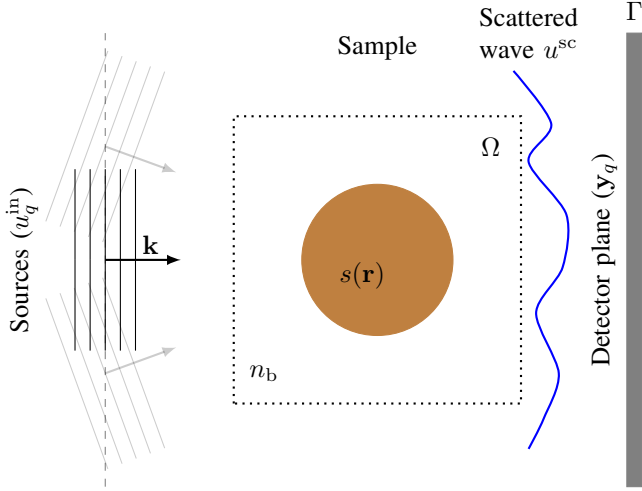


Fig. 2: Optical diffraction tomography. A sample of refractive index $n_b + s(\mathbf{r})$ is immersed in a medium of index n_b and illuminated by an incident plane wave (wave vector \mathbf{k}). The interaction of the wave with the object produces scattered waves, which are recorded at the detector plane.

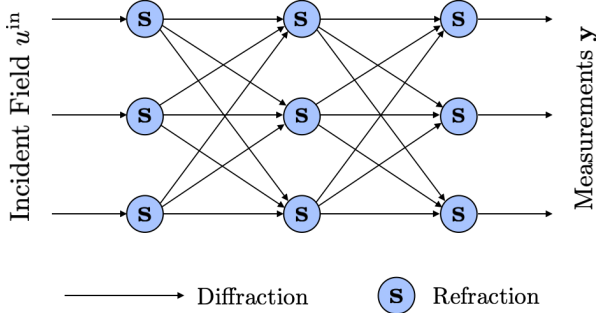


Fig. 3: The computational structure for BPM that resembles a neural network.

the wave vector \mathbf{k} . The total field $u(\mathbf{r})$ resulting from the interaction between the sample and the incident wave is then recorded at the fixed positions $\{\mathbf{r}_m\}_{m=1}^{M'}$ in the detector plane Γ to yield complex measurements $\mathbf{y} \in \mathbb{C}^{M'}$. The interplay between the total field $u(\mathbf{r})$ at any point in space and the refractive index contrast $\delta n(\mathbf{r})$ is described by the Helmholtz equation

$$\nabla^2 u(\mathbf{r}) + k_0^2 n^2(\mathbf{r}) u(\mathbf{r}) = 0, \quad (7)$$

where $k_0 = \frac{2\pi}{\lambda}$.

Beam Propagation Method: For computational purposes, the region of interest Ω is subdivided into a $N_x \times N_z$ array of pixels with sampling steps δ_x and δ_z , respectively. The corresponding samples of the refractive index contrast $s(\mathbf{r})$ and total field $u(\mathbf{r})$ are stored in the vectors $\mathbf{s} \in \mathbb{R}^K$ and $\mathbf{u}^1 \in \mathbb{C}^K$, respectively, where $K = N_x N_z$. Further, let $\mathbf{s}_k \in \mathbb{R}^{N_x}$ and $\mathbf{u}_k \in \mathbb{C}^{N_x}$ represent the above quantities when restricted to the slice $z = k\delta_z$.

¹Since the total field $u(\mathbf{r})$ depends on the refractive index contrast $s(\mathbf{r})$, we also refer to its discretized version as $\mathbf{u}(\mathbf{s})$.

The beam propagation method (BPM) computes the total field \mathbf{u} in a slice-by-slice manner along the z -axis. For a given incident wave $u^{\text{in}}(\mathbf{r})$ that is propagated over a region larger than Ω , we set the initial conditions as $\mathbf{u}_{-1}(\mathbf{s}) = (u^{\text{in}}(x = i\delta_x, z = -\delta_z))_{i=0}^{N_x-1} \in \mathbb{C}^{N_x}$. The total field over Ω is then computed via a series of diffraction and refraction steps

$$\tilde{\mathbf{u}}_k(\mathbf{s}) = \mathbf{u}_{k-1}(\mathbf{s}) * \mathbf{h}_{\text{prop}}^{\delta_z} \quad (\text{diffraction}) \quad (8)$$

$$\mathbf{u}_k(\mathbf{s}) = \tilde{\mathbf{u}}_k(\mathbf{s}) \odot \mathbf{p}_k(\mathbf{s}) \quad (\text{refraction}), \quad (9)$$

where $k = 0, 1, \dots, N_z - 1$, and the symbols $*$ and \odot stand for convolution and pointwise multiplication, respectively. The convolution kernel $\mathbf{h}_{\text{prop}}^{\delta_z} \in \mathbb{C}^{N_x}$ for the diffraction step is characterized in the Fourier domain as

$$\mathcal{F}\{\mathbf{h}_{\text{prop}}^{\delta_z}\} = e^{j\delta_z \left(\sqrt{k_0^2 n_b^2 - \mathbf{w}_x^2} \right)}, \quad (10)$$

where \mathcal{F} denotes the discrete Fourier transform and $\mathbf{w}_x \in \mathbb{R}^{N_x}$ is the frequency variable. The subsequent refraction step involves a pointwise multiplication with the phase mask

$$\mathbf{p}_k(\mathbf{s}) = e^{jk_0 \delta_z s_k}. \quad (11)$$

Finally, we define an operator $\mathbf{R} : \mathbb{C}^{N_x} \mapsto \mathbb{C}^{M'}$ that propagates $\mathbf{u}_{N_z-1}(\mathbf{s})$ to the detector plane Γ and restricts it to the sensor positions to give us the measurements $\mathbf{y} \in \mathbb{C}^{M'}$. Thus, for a given incident wave u^{in} , our noise-free nonlinear BPM forward model is of the form

$$\mathbf{y}_0 = \mathbf{H}_{\text{bpm}}(\mathbf{s}; u^{\text{in}}) = \mathbf{R}(\mathbf{u}_{N_z-1}(\mathbf{s})). \quad (12)$$

In Figure 3, we show the implementation of \mathbf{H}_{bpm} as a directed acyclic graph.

Complete Forward Model: We assume that the sample is illuminated with Q incident plane waves $\{u_q^{\text{in}}\}_{q \in \{1, \dots, Q\}}$ and the corresponding measurements are $\{\mathbf{y}_q \in \mathbb{C}^{M'}\}_{q \in \{1, \dots, Q\}}$. These measurements are related to the RI variation \mathbf{s} of the sample through the BPM forward model in (12). We define a stacked measurement vector as $\mathbf{y} = [\mathbf{y}_1, \dots, \mathbf{y}_Q] \in \mathbb{R}^M$ ($M = QM'$). This allows us to rewrite the complete forward model in the form of (4) where the operator \mathbf{H} consists of applying \mathbf{H}_{bpm} with all the different illuminations and concatenating the outputs into a single vector.

III. BAYESIAN RECONSTRUCTION FRAMEWORK

We now present our reconstruction framework that is based on Bayesian statistics for solving the generic nonlinear inverse problem described in Section II-A. The image \mathbf{s} is assumed to be a realization of a random vector with pdf p_S and the statistical model for measurement noise is included within the likelihood function $p_{Y|S}$, which is the conditional distribution of the measurements given the image. The quantity of interest here is the posterior distribution $p_{S|Y}$ as it provides a complete statistical characterization of the problem at hand. Using Bayes' rule, we then write $p_{S|Y}$ as

$$p_{S|Y}(\mathbf{s}|\mathbf{y}) = \frac{p_{Y|S}(\mathbf{y}|\mathbf{s})p_S(\mathbf{s})}{\int_{\mathbb{R}^K} p_{Y|S}(\mathbf{y}|\mathbf{s})p_S(\mathbf{s})d\mathbf{s}}. \quad (13)$$

In this section, we first characterize the likelihood function $p_{Y|S}$. We then discuss the prior distribution p_S , which in our framework is defined using a deep generative model. Finally, we detail a MCMC scheme to generate samples from the posterior distribution $p_{S|Y}$. This allows us to perform inference by computing point-estimates and the uncertainties associated with them.

A. Likelihood Function

In our framework, we assume that the operator $\mathbf{N} : \mathbf{y}_0 \mapsto \mathbf{N}(\mathbf{y}_0)$ in (4) samples the noisy measurement vector \mathbf{y} from a conditional distribution $p_{Y|Y_0}$, that is,

$$\mathbf{y} \sim p_{Y|Y_0}(\cdot | \mathbf{y}_0 = \mathbf{H}(\mathbf{s})), \quad (14)$$

where $p_{Y|Y_0}$ models the statistics of the noise in the imaging system. Since our forward models \mathbf{H} are deterministic, the quantity $p_{Y|S}$ (a.k.a. the likelihood function) is given by

$$p_{Y|S}(\mathbf{y}|\mathbf{s}) = p_{Y|Y_0}(\mathbf{y}|\mathbf{y}_0 = \mathbf{H}(\mathbf{s})). \quad (15)$$

In many imaging systems, there exist multiple independent sources of noise and so it is reasonable to assume an additive white Gaussian noise model (AWGN) due to the central limit theorem. There, the distribution $p_{Y|Y_0}$ is

$$p_{Y|Y_0}(\mathbf{y}|\mathbf{y}_0) \propto \exp\left(-\frac{\|\mathbf{y} - \mathbf{y}_0\|_2^2}{2\sigma^2}\right), \quad (16)$$

where σ is the standard deviation of the Gaussian noise.

Another model that is commonly used is the shot or Poisson noise model. In this case, we have

$$p_{Y|Y_0}(\mathbf{y}|\mathbf{y}_0) = \prod_{m=1}^M \frac{([y_0]_m)^{[y]_m}}{([y]_m)!} \exp(-[y_0]_m), \quad (17)$$

where $\mathbf{y} \in \mathbb{Z}_+^M$.

B. Prior Distribution

The choice of the distribution p_S reflects our prior knowledge about the image of interest. This information is crucial for the resolution of the inverse problem, especially when it is ill-posed. In the classical Bayesian methods, p_S is usually chosen from a family of distributions with closed-form analytical expressions such that it fits the characteristics of the image and also allows for efficient inference. Popular examples include the Gaussian and Markovian models. Instead, in our framework, we propose to leverage the power of neural networks to define a data-driven prior distribution.

We assume that we have access to a dataset containing sample images from the true unknown probability distribution p_{image} of our image of interest. The idea then is to approximate p_{image} with p_S that is defined by a deep generative model. More specifically, we consider generative models consisting of a generator network $G : \mathbb{R}^d \rightarrow \mathbb{R}^K$ ($d \ll K$) that maps a low-dimensional latent space to the high-dimensional image space. This network takes a vector $\mathbf{z} \in \mathbb{R}^d$, which is sampled from some distribution p_Z (typically a Gaussian or Uniform distribution), as input and yields a sample image $G(\mathbf{z})$ as the

output. Thus, the generator network G and the distribution p_Z implicitly characterize p_S and provide us with a way to directly sample from it. If this model is properly trained, the resulting p_S is close to p_{image} and the generated images are statistically similar to the ones in the dataset.

In our experiments (see Section IV), we use the well-known Wasserstein GANs (WGANs) [85] for our data-driven prior. We provide a brief description of WGANs in Appendix A.

Augmented Deep Generative Priors: Training deep generative models such as GANs requires large amounts of data and is a challenging task in general. Over the past few years, there have been several proposals for improving their performance and this has led to the development of better training schemes and network architectures. Most existing works use normalized datasets, where each image has the same range of pixel values, for their models. However, this is not suitable if we wish to use such models as priors in quantitative imaging (*e.g.*, ODT). In these modalities, it is important to recover the actual values of the object (image) as compared to only the contrast. Thus, we require our generative model to be able to output images with different ranges of pixel values.

While performing our experiments, we observed that training high-quality WGANs on unnormalized datasets was non-trivial. We propose a simple effective workaround, which simplifies the training and allows us to build models that generate images with different ranges. We define an augmented generative model $G_h : \mathbb{R}^{d+1} \rightarrow \mathbb{R}^K$ ($d \ll K$) that consists of a (standard) generative network $G : \mathbb{R}^d \rightarrow \mathbb{R}^K$ trained on a normalized dataset and a deterministic function $h : \mathbb{R} \rightarrow \mathbb{R}$. Here, the latent vector $\mathbf{z} = (\mathbf{z}_1, z_2) \in \mathbb{R}^{d+1}$ has two independent components $\mathbf{z}_1 \in \mathbb{R}^d$ and $z_2 \in \mathbb{R}$ that are sampled from p_{Z_1} and p_{Z_2} respectively, and the output image is given by $G_h(\mathbf{z}) = h(z_2)G(\mathbf{z}_1)$. For a generated image $G_h(\mathbf{z}) \in \mathbb{R}^K$, the term $G(\mathbf{z}_1) \in \mathbb{R}^K$ represents its details or contrast, and the term $h(z_2)$ represents its scaling factor. Since G is now required to only produce images with the same range, we can rely on existing GANs to obtain high-quality models. Moreover, the distribution of the scaling factor can be easily controlled by carefully choosing the distribution p_{Z_2} and the function h .

C. Sampling from the Posterior Distribution

Now that we have described the likelihood function $p_{Y|S}$ and the prior distribution p_S , we look at the problem of drawing samples from the posterior distribution $p_{S|Y}$. Since our prior distribution p_S is defined by a pre-trained augmented deep generative model $G_h : \mathbb{R}^{d+1} \rightarrow \mathbb{R}^K : \mathbf{z} \mapsto G_h(\mathbf{z})$ with $p_Z(\mathbf{z}) = p_{Z_1}(\mathbf{z}_1)p_{Z_2}(z_2)$ for any $\mathbf{z} = (\mathbf{z}_1, z_2) \in \mathbb{R}^{d+1}$, we can focus on the posterior distribution $p_{Z|Y}$ of the latent vector instead. Specifically, if we generate a sample $\bar{\mathbf{z}}$ from $p_{Z|Y}$, then the image $\bar{\mathbf{s}} = G_h(\bar{\mathbf{z}})$ is a sample from $p_{S|Y}$. This is advantageous from a computational point of view as we now have to draw samples in the low-dimensional latent space instead of the high-dimensional image space directly.

In this work, we use the Metropolis-adjusted Langevin algorithm (MALA) [67], [68], which is a Markov Chain Monte

Carlo (MCMC) method, to sample from $p_{Z|Y}$. The general idea in MCMC methods is to design a Markov chain whose stationary (or invariant) distribution is the target distribution that we want to sample from. If the chain is run for a sufficiently long time, the generated samples (after the chain has converged) are indeed samples from the target distribution. The Markov property of the chain implies that each random sample only depends on the previous one.

Given a sample $\bar{\mathbf{z}}_t$, MALA generates the next one $\bar{\mathbf{z}}_{t+1}$ with the help of two steps. First, we construct a proposal $\tilde{\mathbf{z}}_{t+1}$ for the new sample, which is given by

$$\tilde{\mathbf{z}}_{t+1} = \bar{\mathbf{z}}_t + \eta \nabla_{\mathbf{z}} \log p_{Z|Y}(\bar{\mathbf{z}}_t | \mathbf{y}) + \sqrt{2\tau} \zeta, \quad (18)$$

where ζ is drawn from the standard multivariate Gaussian distribution and $\eta \in \mathbb{R}_+$ is a fixed step-size. In the second step, the proposal $\tilde{\mathbf{z}}_{t+1}$ is either accepted or rejected, with the acceptance probability being

$$\alpha = \min \left\{ 1, \frac{p_{Z|Y}(\tilde{\mathbf{z}}_{t+1} | \mathbf{y}) q_{\mathbf{y}}(\bar{\mathbf{z}}_t | \tilde{\mathbf{z}}_{t+1})}{p_{Z|Y}(\bar{\mathbf{z}}_t | \mathbf{y}) q_{\mathbf{y}}(\tilde{\mathbf{z}}_{t+1} | \bar{\mathbf{z}}_t)} \right\}, \quad (19)$$

where $q_{\mathbf{y}}(\bar{\mathbf{z}} | \tilde{\mathbf{z}}) = \exp \left(-\frac{1}{4\tau} \|\bar{\mathbf{z}} - \tilde{\mathbf{z}} - \eta \nabla_{\mathbf{z}} \log p_{Z|Y}(\bar{\mathbf{z}} | \mathbf{y})\|_2^2 \right)$. If the proposal is accepted, we set $\bar{\mathbf{z}}_{t+1} = \tilde{\mathbf{z}}_{t+1}$; otherwise $\bar{\mathbf{z}}_{t+1} = \bar{\mathbf{z}}_t$. The step-size τ is generally chosen to obtain a reasonable acceptance rate for the algorithm. One advantage of MALA is that it uses the gradient of the (log) target distribution to construct more probable proposals. In doing so, it achieves higher acceptance rates compared to other MCMC methods such as the Metropolis-Hastings algorithm [86].

The major computational bottleneck in MALA is the computation of the gradient term $\nabla_{\mathbf{z}} \log p_{Z|Y}$ as it involves terms such as $\mathbf{J}_{\mathbf{H}}^H(\mathbf{x}_1) \mathbf{r}_1$ and $\mathbf{J}_{\mathbf{G}_h}^H(\mathbf{x}_2) \mathbf{r}_2$, where $\mathbf{x}_1 \in \mathbb{R}^K$, $\mathbf{r}_1 \in \mathbb{C}^M$, $\mathbf{x}_2 \in \mathbb{R}^{d+1}$ and $\mathbf{r}_2 \in \mathbb{R}^K$. For instance, if we assume an additive white Gaussian noise model with variance σ^2 and that p_Z is the standard multivariate Gaussian distribution, then $p_{Z|Y}$ can be written as

$$p_{Z|Y}(\mathbf{z} | \mathbf{y}) = \frac{1}{C} \exp \left(-\frac{\|\mathbf{y} - \mathbf{H}\{\mathbf{G}_h(\mathbf{z})\}\|_2^2}{2\sigma^2} - \frac{\|\mathbf{z}\|_2^2}{2} \right), \quad (20)$$

where C is the constant normalizing factor. In this case, the gradient term is

$$\nabla_{\mathbf{z}} \log p_{Z|Y}(\mathbf{z} | \mathbf{y}) = -\frac{\mathbf{J}_{\mathbf{G}_h}^H(\mathbf{z}) \mathbf{J}_{\mathbf{H}}^H(\mathbf{G}_h(\mathbf{z})) (\mathbf{y} - \mathbf{H}\{\mathbf{G}_h(\mathbf{z})\})}{\sigma^2} - \mathbf{z}. \quad (21)$$

Since \mathbf{G}_h is a neural network and \mathbf{H} has a neural-network-like structure, we then compute $\nabla_{\mathbf{z}} \log p_{Z|Y}$ efficiently using an error backpropagation algorithm.

Once we obtain the samples $\{\bar{\mathbf{z}}_t\}_{t=1}^T$ from $p_{Z|Y}$, we transform them to get the samples $\{\mathbf{G}_h(\bar{\mathbf{z}}_t)\}_{t=1}^T$ from $p_{S|Y}$ and then use them to perform inference. Specifically, we approximate any integral of the form $\int_{\mathbb{R}^K} f(\mathbf{s}) p_{S|Y}(\mathbf{s} | \mathbf{y}) d\mathbf{s}$, where $f : \mathbb{R}^K \rightarrow \mathbb{R}$ is a real-valued function, by its empirical estimate $E_T(f) = \frac{1}{T} \sum_{t=1}^T f(\mathbf{G}_h(\bar{\mathbf{z}}_t))$. Although the generated samples are not independent due to the Markov property of the sequence, the Markov Chain Central Limit Theorem [87] ensures that $E_T(f)$ concentrates around the true value of the integral.

In practice, we discard some of the samples generated at

the beginning of the chain in order to allow it to converge to the stationary distribution. This ‘‘burn-in’’ period can often be shortened by choosing a more suitable starting point for the chain instead of a random one. Thus, we initialize MALA with

$$\mathbf{z}_{\text{init}} = \arg \min_{\mathbf{z} \in \mathbb{R}^{d+1}} \|\mathbf{s}_{\text{init}} - \mathbf{G}_h(\mathbf{z})\|_2^2, \quad (22)$$

where \mathbf{s}_{init} is a low-quality estimate obtained by using some fast classical reconstruction algorithm.

IV. EXPERIMENTAL RESULTS

In this section, we show the benefits of our neural-network-based Bayesian reconstruction framework by applying it to both phase retrieval and optical diffraction tomography problems.

A. Augmented WGANs

In our first experiment, we highlight the importance of the proposed augmented generative models. We consider the task of training WGAN models on datasets consisting of 128×128 images, where each image contains a constant-valued disc and its background pixels are zero-valued. The coordinates (x, y) of the center of the disc, its radius r (in pixels) and its constant value v follow the uniform distributions $U_{(10,115)}$, $U_{(10,115)}$, $U_{[4,25]}$ and $U_{(0,0.2]}$ respectively. The aforementioned parameters implicitly define the probability distribution p_{data} that we wish to approximate using WGANs.

We qualitatively compare the performance of two models. The first model is a WGAN trained on 50,000 images sampled from p_{data} . In this case, the distribution p_Z for the latent variable is chosen to be the standard multivariate Gaussian distribution. The second model is an augmented WGAN, where the WGAN component is trained on a normalized dataset with 50,000 images. Thus, we first sample 50,000 images from p_{data} and we then normalize each of them such that the value of the disc is one. The distributions p_{Z_1} and p_{Z_2} are chosen to be standard Gaussian distributions as well, and the function h is

$$h(x) = \frac{0.2}{\sqrt{2\pi}} \int_{-\infty}^x e^{-\frac{t^2}{2}} dt. \quad (23)$$

This choice of h and p_{Z_2} ensures that the scaling factor of the augmented WGAN follows the uniform distribution $U_{(0,0.2]}$. For both the models, we use the generator and critic network architectures shown in Table I. The WGAN is trained for 2500 epochs while the augmented WGAN is trained for 1250 epochs using RMSProp optimizers with a learning rate of 5×10^{-5} and a batch size of 64. The parameters λ_{gp} and n_{critic} (refer to Appendix A) are set as 10 and 5, respectively.

In Figure 4, we present typical samples generated by the two models. We observe that the augmented WGAN, unlike the WGAN, is able to produce sharp piecewise-constant discs.

B. Phase Retrieval

Next, we look at the phase retrieval problem. The ground-truth images for this set of experiments are taken from the MNIST [88] testing dataset which contains 28×28 images

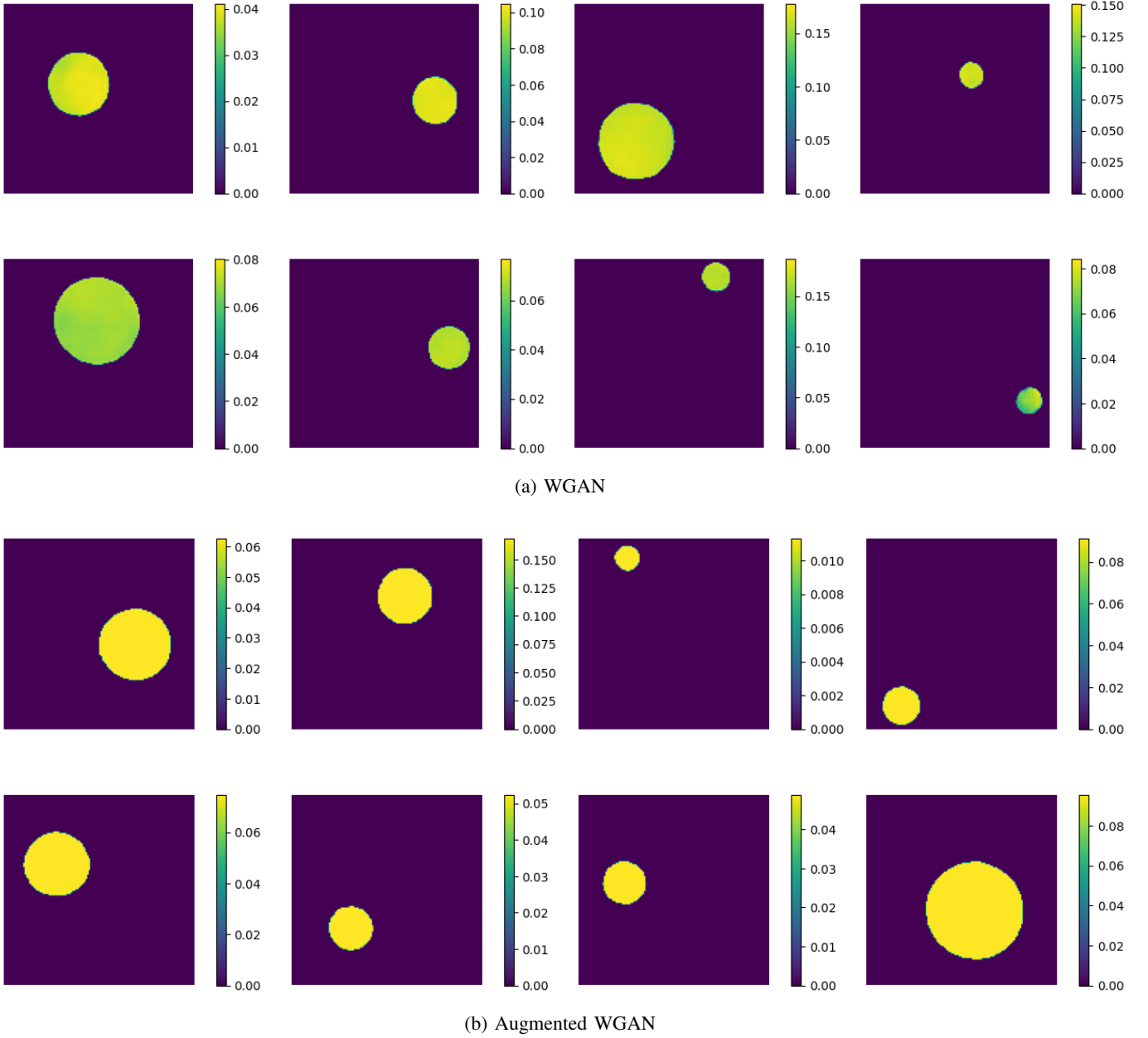


Fig. 4: Samples generated by trained models.

of handwritten digits. The chosen images are normalized to have values in the range $[0, 1]$, and then they are scaled by a factor $\alpha \in (0, 0.5]$. The measurements $\mathbf{y} \in \mathbb{Z}_+^M$ are simulated according to (6) with a Poisson noise model and where \mathbf{A} is a fixed random matrix with i.i.d. entries from a zero-mean Gaussian distribution with variance $\sigma_{\mathbf{A}}^2$.

We use an augmented model G_h to define the prior in our Bayesian framework. The WGAN component is trained on the normalized MNIST training dataset which contains 50,000 images with values in the range $[0, 1]$. The distributions p_{Z_1} and p_{Z_2} are standard Gaussian distributions and the function h is

$$h(x) = \frac{0.5}{\sqrt{2\pi}} \int_{-\infty}^x e^{-\frac{t^2}{2}} dt. \quad (24)$$

The architectures for the generator and critic networks are shown in Table II. The WGAN is trained for 750 epochs using ADAM optimizers with a learning rate of 2×10^{-4} , hyperparameters $(\beta_1, \beta_2) = (0.5, 0.999)$ and a batch size of 64. The parameters λ_{gp} and n_{critic} are set as 10 and 5, respectively.

As discussed in Section III-C, we draw samples from the posterior distribution using MALA. The estimate \mathbf{s}_{init} that we use for initializing the chain is taken to be the solution of a

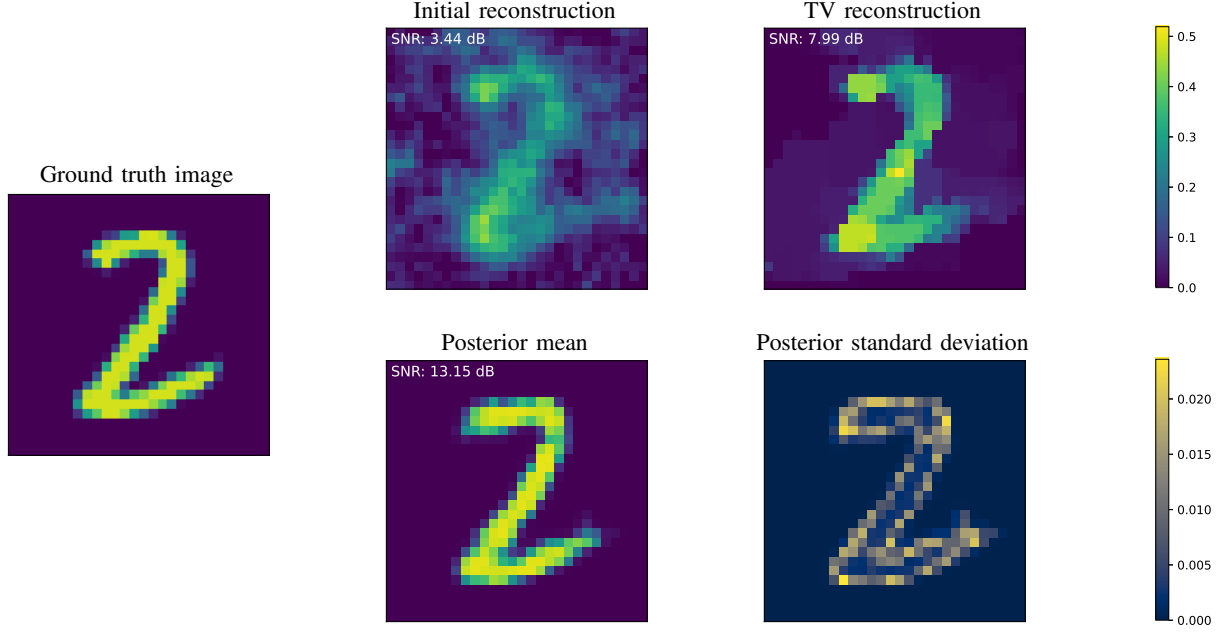


Fig. 5: Reconstructions for phase retrieval: oversampling ratio $M/K = 0.15$.

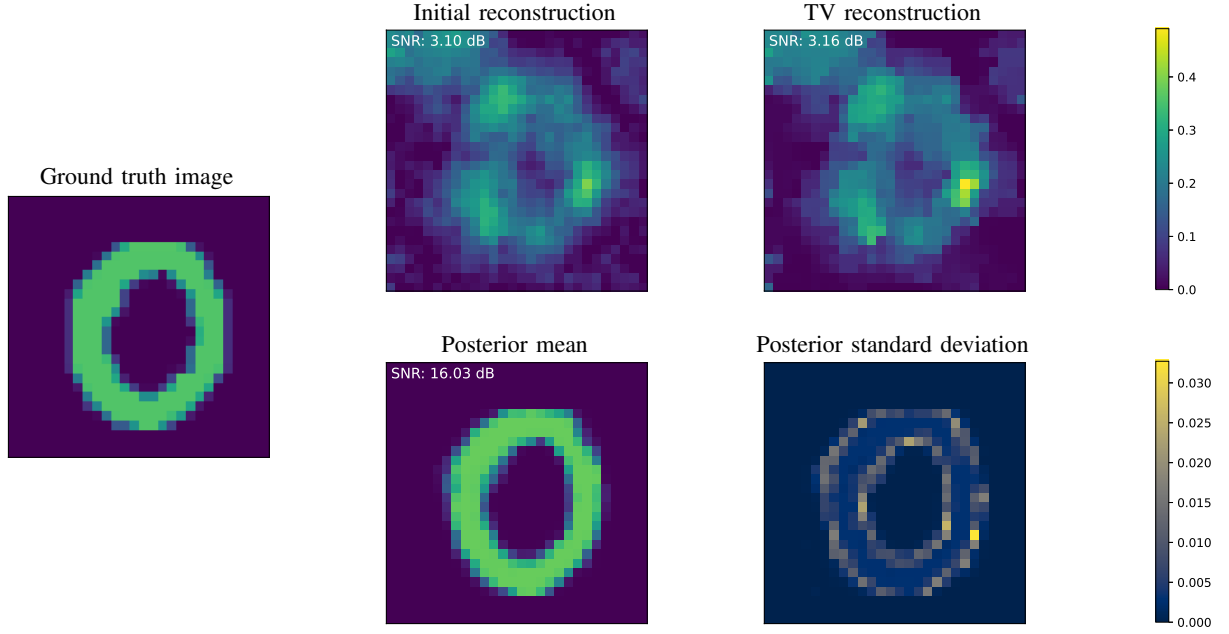


Fig. 6: Reconstructions for phase retrieval: oversampling ratio $M/K = 0.1$.

variational problem with Tikhonov regularization, that is,

$$\mathbf{s}_{\text{init}} = \arg \min_{\mathbf{s} \in \mathbb{R}^K} \left(\sum_{m=1}^M \left(-[\mathbf{y}]_m \log([\mathbf{A}\mathbf{s}]_m^2) + [\mathbf{A}\mathbf{s}]_m^2 \right) + \tau \|\nabla \mathbf{s}\|_{2,2}^2 + i_+(\mathbf{s}) \right), \quad (25)$$

where $\nabla : \mathbb{R}^K \rightarrow \mathbb{R}^{K \times 2}$ is the gradient operator, $\|\cdot\|_{p,q}$ is

the (ℓ_p, ℓ_q) -mixed norm defined as

$$\|\mathbf{x}\|_{p,q} = \left(\sum_{u=1}^U \left(\sum_{v=1}^V ([\mathbf{x}]_{u,v})^p \right)^{q/p} \right)^{1/q} \quad \forall \mathbf{x} \in \mathbb{R}^{U \times V}, \quad (26)$$

$\tau \in \mathbb{R}_+$ is the regularization parameter and the functional i_+ given by

$$i_+(\mathbf{s}) = \begin{cases} 0, & \text{if } \mathbf{s} \in \mathbb{R}_+^K \\ +\infty, & \text{otherwise} \end{cases} \quad (27)$$

enforces the non-negativity constraint on the solution. The

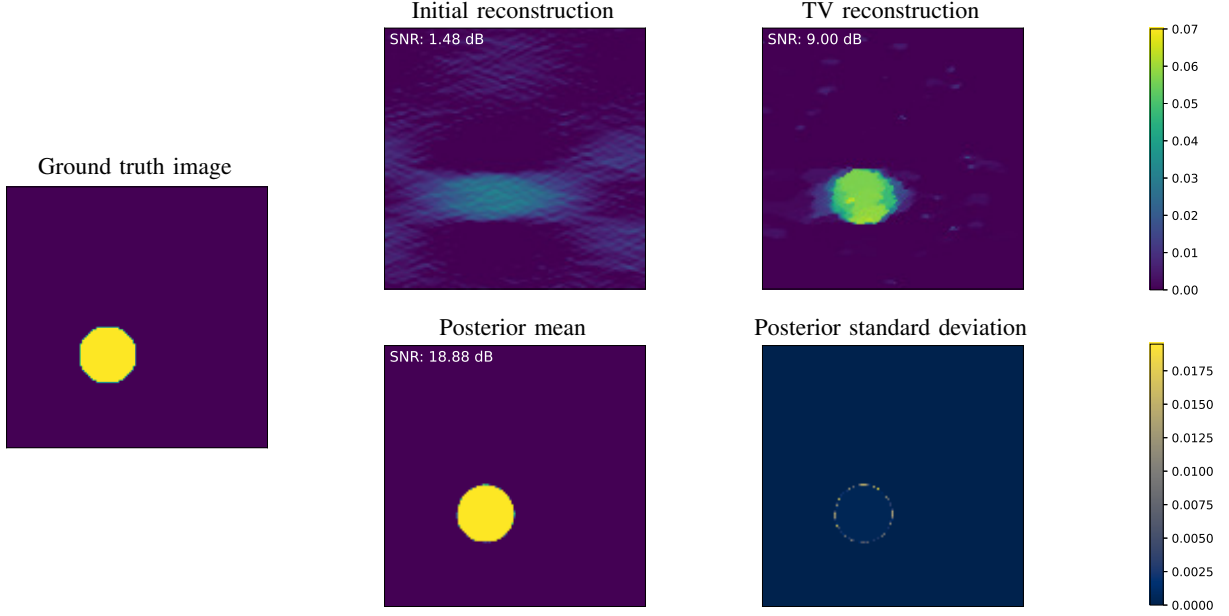


Fig. 7: Reconstructions for ODT: $v = 0.07$, $\theta = \pi/12$, $\sigma_n^2 = 0.05$.

data-fidelity term in (25) corresponds to the negative log-likelihood under the Poisson noise model. We solve Problem (25) using a projected gradient descent algorithm. The optimal regularization parameter τ , in terms of the mean square error (MSE) (with respect to the ground-truth), is chosen via a grid search.

The step-size η for MALA is chosen such that the acceptance probability lies in the range $[0.2, 0.5]$. We discard the first T_b samples in order to allow the Markov chain to converge. After this burn-in period, we collect the next T samples for performing inference. We compute the posterior mean which corresponds to the minimum mean-square error (MMSE) estimate. Further, to quantify the uncertainty associated with our estimation, we also compute the pixelwise standard deviation map.

We compare the performance of our GAN-based posterior mean estimator with that of a TV-regularized method [3]

$$\mathbf{s}_{\text{TV}} = \arg \min_{\mathbf{s} \in \mathbb{R}^K} \left(\sum_{m=1}^M \left(-[\mathbf{y}]_m \log([\mathbf{A}\mathbf{s}]^2)_m + [\mathbf{A}\mathbf{s}]^2_m \right) + \tau \|\nabla \mathbf{s}\|_{2,1} + i_+(\mathbf{s}) \right). \quad (28)$$

TV regularization is known to promote piecewise-constant solutions and is well-matched to our MNIST test images. We solve Problem (28) using FISTA [10] which is initialized with \mathbf{s}_{init} . The regularization parameter τ is tuned for optimal MSE performance with the help of a grid search.

In order to illustrate the advantage of our neural-network-based prior, we consider two extreme imaging settings where the number of measurements M is very small. For the first case (Figure 5), we have $\alpha = 0.4875$, $M/K = 0.15$, $\sigma_{\mathbf{A}}^2 = 2$, $\eta = 5 \times 10^{-6}$, $T_b = 4 \times 10^5$ and $T = 6 \times 10^5$. The parameters for the second case (Figure 6) are $\alpha = 0.36$, $M/K = 0.1$, $\sigma_{\mathbf{A}}^2 =$

10 , $\eta = 10^{-5}$, $T_b = 8 \times 10^5$ and $T = 12 \times 10^5$.

In Figures 5 and 6, we see that the GAN-based posterior mean estimator considerably outperforms the TV-regularized method. Here, the very low oversampling ratios severely affect the performance of TV regularization even though it is a good fit for the underlying images. In fact, the TV reconstruction is barely better than the initial Tikhonov reconstruction for the second case. On the other hand, despite the scarcity of measurements, our estimator remarkably yields excellent results. This highlights the potential of learning-based priors for highly ill-posed problems. Finally, we observe that as one would expect, the standard deviation maps indicate higher uncertainty at the edges for the posterior mean estimator.

C. Optical Diffraction Tomography

For our ODT experiments, the test images (refractive index contrasts) are samples from the dataset described earlier in Section IV-A; that is, piecewise-constant discs with value v . The measurements are simulated using BPM (see Section II-C) with an additive white Gaussian noise model of variance σ_n^2 . We set the sampling steps to $\delta_x = \delta_y = 0.1 \mu\text{m}$, the medium RI to $n_b = 1.52$, and the wavelength to $\lambda = 0.406 \mu\text{m}$. We use Q incident tilted plane waves with angles that are uniformly spaced in the range $[-\theta, \theta]$.

We use the augmented WGAN prior from Section IV-A in our reconstruction framework. Here, the estimate \mathbf{s}_{init} for initializing MALA is obtained by applying a filtered back-propagation algorithm that uses the Rytov approximation [83] for modelling the scattering. We collect T samples from the posterior distribution using MALA with a step-size τ and burn-in period T_b , and use them to compute the posterior mean and pixelwise standard deviation map.

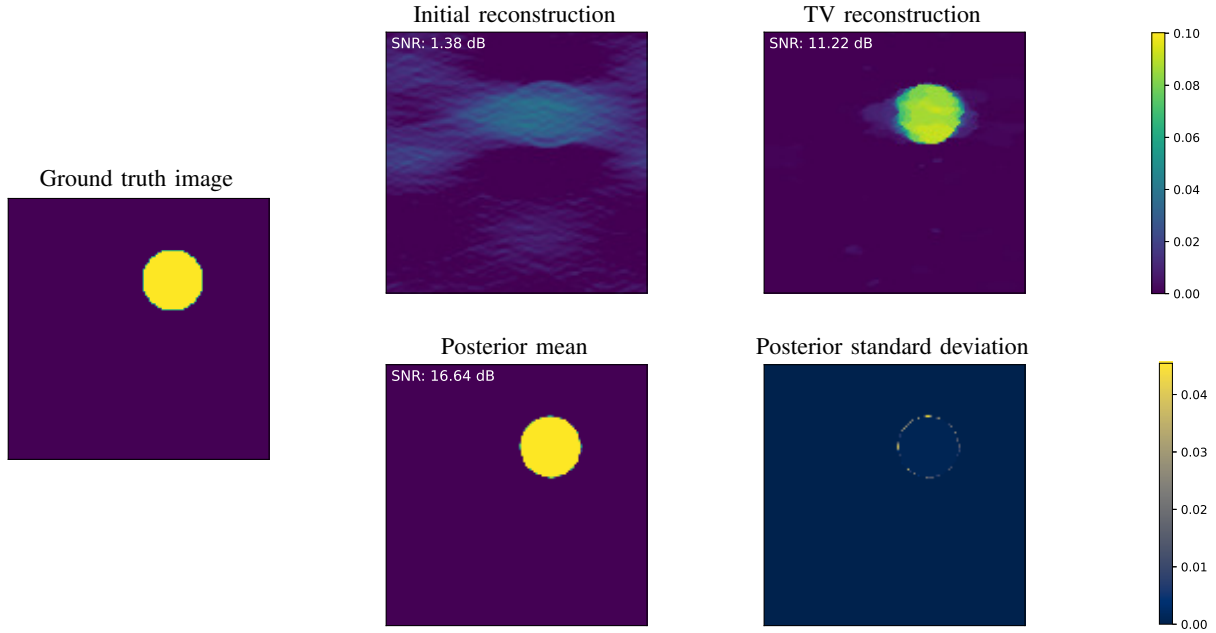


Fig. 8: Reconstructions for ODT: $v = 0.1$, $\theta = \pi/12$, $\sigma_n^2 = 0.05$.

We compare our estimator with the TV-based method

$$\mathbf{s}_{\text{TV}} = \arg \min_{\mathbf{s} \in \mathbb{R}^K} \left(\sum_{q=1}^Q \|\mathbf{y}_q - \mathbf{H}_{\text{bpm}}(\mathbf{s}; u_q^{\text{in}})\|_2^2 + \tau \|\nabla \mathbf{s}\|_{2,1} + i_+(\mathbf{s}) \right), \quad (29)$$

which is well-suited for the piecewise-constant discs in our ground truth images. Problem (29) is solved using FISTA that is initialized with \mathbf{s}_{init} and the regularization parameter τ is tuned for optimal MSE performance via a grid search.

We present results for two highly ill-posed settings where we choose a small value for θ [89]. This means that the incident waves lie in a rather limited range. Thus, the measurements lack some information along the horizontal axis leading to the so-called missing cone problem. For the first case (Figure 7), we have $v = 0.07$, $\theta = \pi/12$, $\sigma_n^2 = 0.05$, $\eta = 2 \times 10^{-7}$, $T_b = 2 \times 10^4$ and $T = 8 \times 10^4$. For the second case (Figure 8), we have $v = 0.1$, $\theta = \pi/12$, $\sigma_n^2 = 0.05$, $\eta = 1 \times 10^{-7}$, $T_b = 16 \times 10^4$ and $T = 4 \times 10^4$.

In Figures 7 and 8, we can see that the TV reconstructions (and the initial ones) are elongated in the horizontal direction due to the lack of information along this axis. However, the GAN-based estimator is able to overcome the missing-cone problem and yields much better reconstructions.

V. CONCLUSION

In this paper, we have presented a Bayesian reconstruction framework for nonlinear inverse problems where the prior information on the image of interest is encoded by a deep generative model. Specifically, we have designed a tractable posterior sampling scheme based on MALA for the class of nonlinear inverse problems where the forward model has

a neural-network-like computational structure. This class includes most practical imaging modalities. We have proposed the concept of augmented generative models that allow us to tackle the problem of quantitative image recovery. Finally, we have illustrated the benefits of our framework by applying it to two nonlinear imaging modalities—phase retrieval and optical diffraction tomography.

APPENDIX A

WASSERSTEIN GENERATIVE ADVERSARIAL NETWORKS (WGANs)

Classical GANs [53] are known to suffer from issues such as the instability of the training process [90], [91], vanishing gradients and mode collapse. The framework of Wasserstein GANs [85] is an alternative that solves these problems.

Let \mathcal{D} be a dataset consisting of samples drawn from a probability distribution p_r . The goal is to build a model using \mathcal{D} that can generate samples which follow a distribution that closely approximates p_r . A WGAN consists of a generator network $G_\theta : \mathbb{R}^d \rightarrow \mathbb{R}^K$ ($d \ll K$), where $\theta \in \mathbb{R}^{d_1}$ denotes its trainable parameters. It takes an input vector $\mathbf{z} \in \mathbb{R}^d$, which is sampled from a fixed distribution p_Z , and outputs $G_\theta(\mathbf{z}) \in \mathbb{R}^K$. The samples generated by this model follow some distribution p_θ that is characterized by G_θ and p_Z . Thus, the parameters θ need to be chosen such that p_θ approximates p_r well.

In the WGAN framework, the generator is trained to minimize the Wasserstein-1 (or Earth-Mover) distance between p_r and p_θ , which is given by

$$W(p_r, p_\theta) = \inf_{\gamma \in \pi(p_r, p_\theta)} \mathbb{E}_{(\mathbf{u}, \mathbf{v}) \sim \gamma} [\|\mathbf{u} - \mathbf{v}\|]. \quad (30)$$

Here, $\pi(p_r, p_\theta)$ is the collection of all joint distributions with marginals p_r and p_θ respectively. The Kantorovich-Rubinstein

Layers	Output shape
Conv 4×4 + LReLU	$512 \times 4 \times 4$
Conv 3×3 + LReLU	$512 \times 4 \times 4$
Upsample	$512 \times 8 \times 8$
Conv 3×3 + LReLU	$512 \times 8 \times 8$
Upsample	$512 \times 16 \times 16$
Conv 3×3 + LReLU	$256 \times 16 \times 16$
Upsample	$256 \times 32 \times 32$
Conv 3×3 + LReLU	$128 \times 32 \times 32$
Upsample	$128 \times 64 \times 64$
Conv 3×3 + LReLU	$64 \times 64 \times 64$
Upsample	$64 \times 128 \times 128$
Conv 3×3 + LReLU	$32 \times 128 \times 128$
Conv 1×1 + Sigmoid	$1 \times 128 \times 128$

(a) Generator network: Input shape is $(128 \times 1 \times 1)$.

Layers	Output shape
Conv 1×1 + LReLU	$16 \times 128 \times 128$
Conv 3×3 + LReLU	$16 \times 128 \times 128$
Conv 3×3 + LReLU	$32 \times 128 \times 128$
Downsample	$32 \times 64 \times 64$
Conv 3×3 + LReLU	$64 \times 64 \times 64$
Downsample	$64 \times 32 \times 32$
Conv 3×3 + LReLU	$128 \times 32 \times 32$
Downsample	$128 \times 16 \times 16$
Conv 3×3 + LReLU	$256 \times 16 \times 16$
Downsample	$256 \times 8 \times 8$
Conv 3×3 + LReLU	$512 \times 8 \times 8$
Downsample	$512 \times 4 \times 4$
Conv 3×3 + LReLU	$512 \times 4 \times 4$
Conv 4×4 + LReLU	$512 \times 1 \times 1$
Fully-connected	$1 \times 1 \times 1$

(b) Critic network: Input shape is $(1 \times 128 \times 128)$.

TABLE I: The generator and critic architectures for the dataset consisting of piecewise-constant discs. The negative slope for LReLU is set as 0.2. The upsampling layer uses nearest neighbor interpolation while the downsampling layer involves max pooling.

duality theorem [92] states that (30) can be written as

$$W(p_r, p_\theta) = \sup_{f \in \mathcal{X}} \mathbb{E}_{\mathbf{u} \sim p_r}[f(\mathbf{u})] - \mathbb{E}_{\mathbf{v} \sim p_\theta}[f(\mathbf{v})], \quad (31)$$

where $\mathcal{X} = \{f : \mathbb{R}^K \rightarrow \mathbb{R} \mid f \text{ is 1-Lipschitz}\}$. The space \mathcal{X} is then replaced by a family of 1-Lipschitz functions represented by a critic neural network $D_\phi : \mathbb{R}^K \rightarrow \mathbb{R}$ with appropriately constrained parameters $\phi \in \mathbb{R}^{d_2}$. This leads to the following minimax problem for training the model:

$$\min_{\theta \in \mathbb{R}^{d_1}} \max_{\phi \in \mathcal{Y}} \mathbb{E}_{\mathbf{u} \sim p_r}[D_\phi(\mathbf{u})] - \mathbb{E}_{\mathbf{v} \sim p_\theta}[D_\phi(\mathbf{v})], \quad (32)$$

where $\mathcal{Y} = \{\phi \in \mathbb{R}^{d_2} \mid D_\phi \text{ is 1-Lipschitz}\}$. In [85], the authors enforce the 1-Lipschitz condition on D_ϕ by clipping its weights during training. However, as shown in [93], this approach can cause difficulties in the optimization process. Instead, the 1-Lipschitz constraint can be enforced by adding

Layers	Output shape
Fully-connected + LReLU	1×128
Fully-connected + Batch-norm + LReLU	1×256
Fully-connected + Batch-norm + LReLU	1×512
Fully-connected + Batch-norm + LReLU	1×1024
Fully-connected + Sigmoid	1×784

(a) Generator network: Input shape is (1×100) .

Layers	Output shape
Fully-connected + LReLU	1×512
Fully-connected + LReLU	1×256
Fully-connected	1×1

(b) Critic network: Input shape is (1×784) .

TABLE II: The generator and critic architectures for the MNIST dataset. The negative slope for LReLU is set as 0.2.

a gradient penalty to the cost function in (32). The regularized minimax problem is

$$\min_{\theta \in \mathbb{R}^{d_1}} \max_{\phi \in \mathbb{R}^{d_2}} \left(\mathbb{E}_{\mathbf{u} \sim p_r}[D_\phi(\mathbf{u})] - \mathbb{E}_{\mathbf{v} \sim p_\theta}[D_\phi(\mathbf{v})] + \lambda_{\text{gp}} \mathbb{E}_{\mathbf{w} \sim p_{\text{int}}} [(\|\nabla_{\mathbf{w}} D_\phi(\mathbf{w})\| - 1)^2] \right), \quad (33)$$

where a point $\mathbf{w} \sim p_{\text{int}}$ is obtained by sampling uniformly along straight lines between points drawn from p_r and p_θ , and $\lambda_{\text{gp}} > 0$ is a hyperparameter.

In practice, Problem (33) is solved using mini-batch stochastic gradient algorithms in an alternating manner. During each iteration for the critic, we collect a batch of samples $\{\mathbf{x}_n\}_{n=1}^{N_c}$ from the dataset \mathcal{D} . We sample vectors $\{\mathbf{z}_n\}_{n=1}^{N_c}$ from p_Z and a sequence of numbers $\{\alpha_n\}_{n=1}^{N_c}$ from the uniform distribution $U_{[0,1]}$, and we construct $\mathbf{w}_n = \alpha_n \mathbf{x}_n + (1 - \alpha_n) G_\theta(\mathbf{z}_n)$. The critic parameters are then updated by ascending along the gradient given by

$$\frac{1}{N_c} \nabla_\phi \left(\sum_{n=1}^{N_c} D_\phi(\mathbf{x}_n) - D_\phi(G_\theta(\mathbf{z}_n)) + \lambda_{\text{gp}} (\|\nabla_{\mathbf{w}_n} D_\phi(\mathbf{w}_n)\| - 1)^2 \right). \quad (34)$$

During each iteration for the generator, we sample latent vectors $\{\mathbf{z}_n\}_{n=1}^{N_g}$ from p_Z . The generator parameters are then updated by descending along the gradient given by

$$\frac{1}{N_g} \nabla_\theta \left(\sum_{n=1}^{N_g} -D_\phi(G_\theta(\mathbf{z}_n)) \right). \quad (35)$$

Typically, for every generator iteration, the critic is trained for n_{critic} iterations.

APPENDIX B WGAN ARCHITECTURES

The generator and critic architectures used for the dataset consisting of piecewise-constant discs are shown in Table I while the architectures used for the MNIST dataset are shown in Table II.

REFERENCES

- [1] A. N. Tikhonov, "Solution of incorrectly formulated problems and the regularization method," *Soviet Mathematics*, vol. 4, pp. 1035–1038, 1963.
- [2] M. Bertero and P. Boccacci, *Introduction to Inverse Problems in Imaging*. CRC press, 1998.
- [3] L. I. Rudin, S. Osher, and E. Fatemi, "Nonlinear total variation based noise removal algorithms," *Physica D: nonlinear phenomena*, vol. 60, no. 1-4, pp. 259–268, 1992.
- [4] M. Lustig, D. L. Donoho, and J. M. Pauly, "Sparse MRI: The application of compressed sensing for rapid MR imaging," vol. 58, no. 6, pp. 1182–1195, Dec. 2007.
- [5] M. Figueiredo, R. Nowak, and S. Wright, "Gradient projection for sparse reconstruction: Application to compressed sensing and other inverse problems," *IEEE Journal of Selected Topics in Signal Processing*, vol. 1, no. 4, pp. 586–597, Dec. 2007.
- [6] J. Lim, K. Lee, K. H. Jin, S. Shin, S. Lee, Y. Park, and J. C. Ye, "Comparative study of iterative reconstruction algorithms for missing cone problems in optical diffraction tomography," *Optics express*, vol. 23, no. 13, pp. 16 933–16 948, 2015.
- [7] U. S. Kamilov, I. N. Papadopoulos, M. H. Shoreh, A. Goy, C. Vonesch, M. Unser, and D. Psaltis, "Optical tomographic image reconstruction based on beam propagation and sparse regularization," *IEEE Transactions on Computational Imaging*, vol. 2, no. 1, pp. 59–70, 2016.
- [8] M. A. Figueiredo and R. D. Nowak, "An em algorithm for wavelet-based image restoration," *IEEE Transactions on Image Processing*, vol. 12, no. 8, pp. 906–916, 2003.
- [9] I. Daubechies, M. Defrise, and C. De Mol, "An iterative thresholding algorithm for linear inverse problems with a sparsity constraint," *Communications on Pure and Applied Mathematics: A Journal Issued by the Courant Institute of Mathematical Sciences*, vol. 57, no. 11, pp. 1413–1457, 2004.
- [10] A. Beck and M. Teboulle, "A fast iterative shrinkage-thresholding algorithm for linear inverse problems," *SIAM journal on imaging sciences*, vol. 2, no. 1, pp. 183–202, 2009.
- [11] S. Boyd, N. Parikh, and E. Chu, *Distributed optimization and statistical learning via the alternating direction method of multipliers*. Now Publishers Inc, 2011.
- [12] A. Mohammad-Djafari, "A full bayesian approach for inverse problems," in *Maximum entropy and Bayesian methods*. Springer, 1996, pp. 135–144.
- [13] —, "Bayesian inference for inverse problems," in *AIP Conference Proceedings*, vol. 617, no. 1. American Institute of Physics, 2002, pp. 477–496.
- [14] A. M. Stuart, "Inverse problems: a bayesian perspective," *Acta numerica*, vol. 19, pp. 451–559, 2010.
- [15] M. Dashti and A. M. Stuart, "The bayesian approach to inverse problems," *arXiv preprint arXiv:1302.6989*, 2013.
- [16] S. D. Babacan, R. Molina, and A. K. Katsaggelos, "Bayesian compressive sensing using laplace priors," *IEEE Transactions on image processing*, vol. 19, no. 1, pp. 53–63, 2009.
- [17] M. Unser and P. D. Tafti, "Stochastic models for sparse and piecewise-smooth signals," *IEEE Transactions on Signal Processing*, vol. 59, no. 3, pp. 989–1006, 2010.
- [18] R. Gribonval, "Should penalized least squares regression be interpreted as maximum a posteriori estimation?" *IEEE Transactions on Signal Processing*, vol. 59, no. 5, pp. 2405–2410, 2011.
- [19] W. R. Gilks, S. Richardson, and D. Spiegelhalter, *Markov chain Monte Carlo in practice*. CRC press, 1995.
- [20] C. J. Geyer, "Practical markov chain monte carlo," *Statistical science*, pp. 473–483, 1992.
- [21] M. Pereyra, P. Schniter, E. Chouzenoux, J.-C. Pesquet, J.-Y. Tourneret, A. O. Hero, and S. McLaughlin, "A survey of stochastic simulation and optimization methods in signal processing," *IEEE Journal of Selected Topics in Signal Processing*, vol. 10, no. 2, pp. 224–241, 2015.
- [22] J. Kaipio and E. Somersalo, *Statistical and computational inverse problems*. Springer Science & Business Media, 2006, vol. 160.
- [23] K. H. Jin, M. T. McCann, E. Froustey, and M. Unser, "Deep convolutional neural network for inverse problems in imaging," *IEEE Transactions on Image Processing*, vol. 26, no. 9, pp. 4509–4522, 2017.
- [24] H. Chen, Y. Zhang, M. K. Kalra, F. Lin, Y. Chen, P. Liao, J. Zhou, and G. Wang, "Low-dose ct with a residual encoder-decoder convolutional neural network," *IEEE transactions on medical imaging*, vol. 36, no. 12, pp. 2524–2535, 2017.
- [25] C. M. Hyun, H. P. Kim, S. M. Lee, S. Lee, and J. K. Seo, "Deep learning for undersampled mri reconstruction," *Physics in Medicine & Biology*, vol. 63, no. 13, p. 135007, 2018.
- [26] K. Monakhova, J. Yurtsever, G. Kuo, N. Antipa, K. Yanny, and L. Waller, "Learned reconstructions for practical mask-based lensless imaging," *Optics express*, vol. 27, no. 20, pp. 28 075–28 090, 2019.
- [27] D. Perdios, M. Vonlanthen, F. Martinez, M. Arditi, and J.-P. Thiran, "Cnn-based image reconstruction method for ultrafast ultrasound imaging," *arXiv preprint arXiv:2008.12750*, 2020.
- [28] K. Gregor and Y. LeCun, "Learning fast approximations of sparse coding," in *Proceedings of the 27th international conference on international conference on machine learning*, 2010, pp. 399–406.
- [29] Y. Chen and T. Pock, "Trainable nonlinear reaction diffusion: A flexible framework for fast and effective image restoration," *IEEE transactions on pattern analysis and machine intelligence*, vol. 39, no. 6, pp. 1256–1272, 2016.
- [30] J. Sun, H. Li, Z. Xu *et al.*, "Deep admm-net for compressive sensing mri," *Advances in neural information processing systems*, vol. 29, 2016.
- [31] H. K. Aggarwal, M. P. Mani, and M. Jacob, "Modl: Model-based deep learning architecture for inverse problems," *IEEE transactions on medical imaging*, vol. 38, no. 2, pp. 394–405, 2018.

- [32] J. Adler and O. Öktem, “Learned primal-dual reconstruction,” *IEEE transactions on medical imaging*, vol. 37, no. 6, pp. 1322–1332, 2018.
- [33] V. Monga, Y. Li, and Y. C. Eldar, “Algorithm unrolling: Interpretable, efficient deep learning for signal and image processing,” *IEEE Signal Processing Magazine*, vol. 38, no. 2, pp. 18–44, 2021.
- [34] V. Antun, F. Renna, C. Poon, B. Adcock, and A. C. Hansen, “On instabilities of deep learning in image reconstruction and the potential costs of ai,” *Proceedings of the National Academy of Sciences*, vol. 117, no. 48, pp. 30088–30095, 2020.
- [35] N. M. Gottschling, V. Antun, B. Adcock, and A. C. Hansen, “The troublesome kernel: why deep learning for inverse problems is typically unstable,” *arXiv preprint arXiv:2001.01258*, 2020.
- [36] S. V. Venkatakrishnan, C. A. Bouman, and B. Wohlberg, “Plug-and-play priors for model based reconstruction,” in *2013 IEEE Global Conference on Signal and Information Processing*. IEEE, 2013, pp. 945–948.
- [37] Y. Romano, M. Elad, and P. Milanfar, “The little engine that could: Regularization by denoising (red),” *SIAM Journal on Imaging Sciences*, vol. 10, no. 4, pp. 1804–1844, 2017.
- [38] T. Ttirer and R. Giryes, “Image restoration by iterative denoising and backward projections,” *IEEE Transactions on Image Processing*, vol. 28, no. 3, pp. 1220–1234, 2018.
- [39] E. K. Ryu, J. Liu, S. Wang, X. Chen, Z. Wang, and W. Yin, “Plug-and-play methods provably converge with properly trained denoisers,” *arXiv preprint arXiv:1905.05406*, 2019.
- [40] Y. Sun, J. Liu, and U. Kamilov, “Block coordinate regularization by denoising,” in *Advances in Neural Information Processing Systems*, 2019, pp. 382–392.
- [41] Z. Wu, Y. Sun, A. Matlock, J. Liu, L. Tian, and U. S. Kamilov, “Simba: scalable inversion in optical tomography using deep denoising priors,” *IEEE Journal of Selected Topics in Signal Processing*, 2020.
- [42] J. Liu, Y. Sun, C. Eldeniz, W. Gan, H. An, and U. S. Kamilov, “Rare: Image reconstruction using deep priors learned without ground truth,” *IEEE Journal of Selected Topics in Signal Processing*, 2020.
- [43] K. Zhang, Y. Li, W. Zuo, L. Zhang, L. Van Gool, and R. Timofte, “Plug-and-play image restoration with deep denoiser prior,” *IEEE Transactions on Pattern Analysis and Machine Intelligence*, 2021.
- [44] Y. Sun, Z. Wu, X. Xu, B. Wohlberg, and U. S. Kamilov, “Scalable plug-and-play admm with convergence guarantees,” *IEEE Transactions on Computational Imaging*, 2021.
- [45] J. Rick Chang, C.-L. Li, B. Poczoz, B. Vijaya Kumar, and A. C. Sankaranarayanan, “One network to solve them all—solving linear inverse problems using deep projection models,” in *Proceedings of the IEEE International Conference on Computer Vision*, 2017, pp. 5888–5897.
- [46] H. Gupta, K. H. Jin, H. Q. Nguyen, M. T. McCann, and M. Unser, “Cnn-based projected gradient descent for consistent ct image reconstruction,” *IEEE transactions on medical imaging*, vol. 37, no. 6, pp. 1440–1453, 2018.
- [47] F. Yang, T.-a. Pham, H. Gupta, M. Unser, and J. Ma, “Deep-learning projector for optical diffraction tomography,” *Optics express*, vol. 28, no. 3, pp. 3905–3921, 2020.
- [48] H. H. Bauschke and P. L. Combettes, *Convex Analysis and Monotone Operator Theory in Hilbert Spaces*, 2nd ed., ser. CMS Books in Mathematics. Springer, Cham, Feb. 2017.
- [49] J. Hertrich, S. Neumayer, and G. Steidl, “Convolutional proximal neural networks and plug-and-play algorithms,” *Linear Algebra and its Applications*, vol. 631, pp. 203–234, Dec. 2021.
- [50] M. Terris, A. Repetti, J.-C. Pesquet, and Y. Wiaux, “Building firmly nonexpansive convolutional neural networks,” in *ICASSP 2020-2020 IEEE International Conference on Acoustics, Speech and Signal Processing (ICASSP)*. IEEE, 2020, pp. 8658–8662.
- [51] P. Bohra, D. Perdios, A. Goujon, S. Emery, and M. Unser, “Learning lipschitz-controlled activation functions in neural networks for plug-and-play image reconstruction methods,” in *NeurIPS 2021 Workshop on Deep Learning and Inverse Problems*, 2021. [Online]. Available: <https://openreview.net/forum?id=efCsbTzQTbH>
- [52] D. P. Kingma and M. Welling, “Auto-encoding variational bayes,” *arXiv preprint arXiv:1312.6114*, 2013.
- [53] I. Goodfellow, J. Pouget-Abadie, M. Mirza, B. Xu, D. Warde-Farley, S. Ozair, A. Courville, and Y. Bengio, “Generative adversarial nets,” *Advances in neural information processing systems*, vol. 27, 2014.
- [54] A. Bora, A. Jalal, E. Price, and A. G. Dimakis, “Compressed sensing using generative models,” in *International Conference on Machine Learning*. PMLR, 2017, pp. 537–546.
- [55] V. Shah and C. Hegde, “Solving linear inverse problems using gan priors: An algorithm with provable guarantees,” in *2018 IEEE international conference on acoustics, speech and signal processing (ICASSP)*. IEEE, 2018, pp. 4609–4613.
- [56] M. Gonzalez, A. Almansa, M. Delbracio, P. Musé, and P. Tan, “Solving inverse problems by joint posterior maximization with a vae prior,” *arXiv preprint arXiv:1911.06379*, 2019.
- [57] W. Huang, P. Hand, R. Heckel, and V. Voroninski, “A provably convergent scheme for compressive sensing under random generative priors,” *Journal of Fourier Analysis and Applications*, vol. 27, no. 2, pp. 1–34, 2021.
- [58] J. Adler and O. Öktem, “Deep bayesian inversion,” *arXiv preprint arXiv:1811.05910*, 2018.
- [59] Z. Kadhodaie and E. P. Simoncelli, “Solving linear inverse problems using the prior implicit in a denoiser,” *arXiv preprint arXiv:2007.13640*, 2020.
- [60] B. Kavar, G. Vaksman, and M. Elad, “Snips: Solving noisy inverse problems stochastically,” *arXiv preprint arXiv:2105.14951*, 2021.
- [61] R. Laumont, V. De Bortoli, A. Almansa, J. Delon, A. Durmus, and M. Pereyra, “Bayesian imaging using

- plug & play priors: when langevin meets tweedie,” *arXiv preprint arXiv:2103.04715*, 2021.
- [62] D. Patel and A. A. Oberai, “Bayesian inference with generative adversarial network priors,” *arXiv preprint arXiv:1907.09987*, 2019.
- [63] K. C. Tezcan, C. F. Baumgartner, and E. Konukoglu, “Sampling possible reconstructions of undersampled acquisitions in mr imaging,” *arXiv preprint arXiv:2010.00042*, 2020.
- [64] M. Holden, M. Pereyra, and K. C. Zygalakis, “Bayesian imaging with data-driven priors encoded by neural networks: Theory, methods, and algorithms,” *arXiv preprint arXiv:2103.10182*, 2021.
- [65] A. Jalal, M. Arvinte, G. Daras, E. Price, A. G. Dimakis, and J. Tamir, “Robust compressed sensing mri with deep generative priors,” *Advances in Neural Information Processing Systems*, vol. 34, pp. 14 938–14 954, 2021.
- [66] Y. Song, L. Shen, L. Xing, and S. Ermon, “Solving inverse problems in medical imaging with score-based generative models,” *arXiv preprint arXiv:2111.08005*, 2021.
- [67] G. O. Roberts and R. L. Tweedie, “Exponential convergence of langevin distributions and their discrete approximations,” *Bernoulli*, pp. 341–363, 1996.
- [68] G. O. Roberts and O. Stramer, “Langevin diffusions and metropolis-hastings algorithms,” *Methodology and computing in applied probability*, vol. 4, no. 4, pp. 337–357, 2002.
- [69] Y. Shechtman, Y. C. Eldar, O. Cohen, H. N. Chapman, J. Miao, and M. Segev, “Phase retrieval with application to optical imaging: a contemporary overview,” *IEEE signal processing magazine*, vol. 32, no. 3, pp. 87–109, 2015.
- [70] F. Fogel, I. Waldspurger, and A. d’Aspremont, “Phase retrieval for imaging problems,” *Mathematical programming computation*, vol. 8, no. 3, pp. 311–335, 2016.
- [71] R. P. Millane, “Phase retrieval in crystallography and optics,” *JOSA A*, vol. 7, no. 3, pp. 394–411, 1990.
- [72] A. M. Maiden and J. M. Rodenburg, “An improved ptychographical phase retrieval algorithm for diffractive imaging,” *Ultramicroscopy*, vol. 109, no. 10, pp. 1256–1262, 2009.
- [73] J. R. Fienup, J. C. Marron, T. J. Schulz, and J. H. Seldin, “Hubble space telescope characterized by using phase-retrieval algorithms,” *Applied optics*, vol. 32, no. 10, pp. 1747–1767, 1993.
- [74] W. L. Freedman, B. F. Madore, B. K. Gibson, L. Ferrarese, D. D. Kelson, S. Sakai, J. R. Mould, R. C. Kennicutt Jr, H. C. Ford, J. A. Graham *et al.*, “Final results from the hubble space telescope key project to measure the hubble constant,” *The Astrophysical Journal*, vol. 553, no. 1, p. 47, 2001.
- [75] M. H. Maleki and A. J. Devaney, “Phase-retrieval and intensity-only reconstruction algorithms for optical diffraction tomography,” *JOSA A*, vol. 10, no. 5, pp. 1086–1092, 1993.
- [76] T. E. Gureyev and K. A. Nugent, “Rapid quantitative phase imaging using the transport of intensity equation,” *Optics communications*, vol. 133, no. 1-6, pp. 339–346, 1997.
- [77] F. Zernike, “Phase contrast, a new method for the microscopic observation of transparent objects part ii,” *Physica*, vol. 9, no. 10, pp. 974–986, 1942.
- [78] G. Zheng, R. Horstmeyer, and C. Yang, “Wide-field, high-resolution fourier ptychographic microscopy,” *Nature photonics*, vol. 7, no. 9, pp. 739–745, 2013.
- [79] J. M. Rodenburg and H. M. Faulkner, “A phase retrieval algorithm for shifting illumination,” *Applied physics letters*, vol. 85, no. 20, pp. 4795–4797, 2004.
- [80] E. J. Candes, X. Li, and M. Soltanolkotabi, “Phase retrieval via wirtinger flow: Theory and algorithms,” *IEEE Transactions on Information Theory*, vol. 61, no. 4, pp. 1985–2007, 2015.
- [81] M. Mondelli and A. Montanari, “Fundamental limits of weak recovery with applications to phase retrieval,” in *Conference On Learning Theory*. PMLR, 2018, pp. 1445–1450.
- [82] E. Wolf, “Three-dimensional structure determination of semi-transparent objects from holographic data,” *Optics Communications*, vol. 1, no. 4, pp. 153–156, 1969.
- [83] A. Devaney, “Inverse-scattering theory within the rytov approximation,” *Optics letters*, vol. 6, no. 8, pp. 374–376, 1981.
- [84] E. Soubies, T.-A. Pham, and M. Unser, “Efficient inversion of multiple-scattering model for optical diffraction tomography,” *Optics express*, vol. 25, no. 18, pp. 21 786–21 800, 2017.
- [85] M. Arjovsky, S. Chintala, and L. Bottou, “Wasserstein generative adversarial networks,” in *International conference on machine learning*. PMLR, 2017, pp. 214–223.
- [86] W. K. Hastings, “Monte carlo sampling methods using markov chains and their applications,” 1970.
- [87] M. I. Gordin and B. A. Lifšic, “The central limit theorem for stationary markov processes,” in *Doklady Akademii Nauk*, vol. 239, no. 4. Russian Academy of Sciences, 1978, pp. 766–767.
- [88] Y. LeCun, L. Bottou, Y. Bengio, and P. Haffner, “Gradient-based learning applied to document recognition,” *Proceedings of the IEEE*, vol. 86, no. 11, pp. 2278–2324, 1998.
- [89] A. Goy, G. Rughoobur, S. Li, K. Arthur, A. I. Akinwande, and G. Barbastathis, “High-resolution limited-angle phase tomography of dense layered objects using deep neural networks,” *Proceedings of the National Academy of Sciences*, vol. 116, no. 40, pp. 19 848–19 856, 2019.
- [90] T. Salimans, I. Goodfellow, W. Zaremba, V. Cheung, A. Radford, and X. Chen, “Improved techniques for training gans,” *Advances in neural information processing systems*, vol. 29, pp. 2234–2242, 2016.
- [91] M. Arjovsky and L. Bottou, “Towards principled methods for training generative adversarial networks,” *arXiv preprint arXiv:1701.04862*, 2017.
- [92] C. Villani, *Optimal transport: old and new*. Springer, 2009, vol. 338.
- [93] I. Gulrajani, F. Ahmed, M. Arjovsky, V. Dumoulin, and

A. Courville, “Improved training of wasserstein gans,”
arXiv preprint arXiv:1704.00028, 2017.